A Mo_2C/Carbon Nanotube Composite Cathode for Lithium–Oxygen Batteries with High Energy Efficiency and Long Cycle Life

Won-Jin Kwak,[†] Kah Chun Lau,[‡] Chang-Dae Shin,[†] Khalil Amine,[§] Larry A Curtiss,[*,‡] and Yang-Kook Sun[*,†]

[†]Department of Energy Engineering, Hanyang University, Seoul, 133-791, Republic of Korea and [‡]Materials Science Division and [§]Chemical Sciences and Engineering Division, Argonne National Laboratory, 9700 South Cass Avenue, Lemont, Illinois 60439, United States

ABSTRACT Although lithium–oxygen batteries are attracting considerable attention because of the potential for an extremely high energy density, their practical use has been restricted owing to a low energy efficiency and poor cycle life compared to lithium-ion batteries. Here we present a nanostructured cathode based on molybdenum carbide nanoparticles (Mo_2C) dispersed on carbon nanotubes, which dramatically increase the electrical efficiency up to 88% with a cycle life of more than 100 cycles. We found that the Mo_2C nanoparticle catalysts contribute to the formation of well-dispersed lithium peroxide nanolayers (Li_2O_2) on the Mo_2C/carbon nanotubes with a large contact area during the oxygen reduction reaction (ORR). This Li_2O_2 structure can be decomposed at low potential upon the oxygen evolution reaction (OER) by avoiding the energy loss associated with the decomposition of the typical Li_2O_2 discharge products.

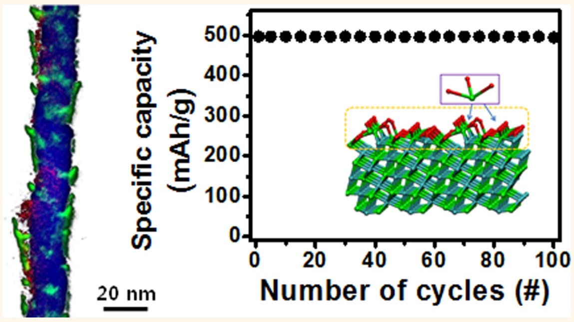

KEYWORDS: lithium oxygen batteries · nanostructures · molybdenum carbide nanoparticles · carbon nanotube · oxygen evolution reaction

Recently, $Li-O_2$ batteries have attracted a considerable amount of interest as an alternative energy storage system for the next generation electrical energy storage, since they possess a much higher theoretical specific energy density (3505 W h kg^{-1}) compared to traditional lithium/sodium batteries and other battery systems. Lithium–oxygen batteries are based on the electrochemical reaction $2Li^+ + 2e^- + O_2 \leftrightarrow Li_2O_2$, $E^o = 2.96$ V.[1,2] The five times larger energy density compared to Li-ion batteries and its environment friendly reaction system make $Li-O_2$ batteries a promising energy storage system for electric-vehicle applications. Despite their great prospect, practical use of $Li-O_2$ batteries still suffer many challenges such as low energy efficiency, poor rate capability, and a poor cycle life. These problems are mainly attributable to excessive accumulation of discharge products (e.g., nonconductive Li_2O_2), which induce poor reversibility and high polarization when they decompose during charging.[3,4] Consequently, the number of operating cycles for $Li-O_2$ batteries cannot yet match those of Li-ion batteries. Moreover, the energy efficiency (<80%) of the present $Li-O_2$ battery system is also too low. To improve the performance of $Li-O_2$ battery systems, a key factor is finding ways to enhance the catalytic activity of the cathode for formation and decomposition of Li_2O_2, which is critical to decrease the polarization and increase the reversibility.[5,6] Proper electrode design is important because it can result in effective control of the morphology of the discharge products.[7,8] For these reasons, among the components of Li–air batteries, the cathode plays a key role in the performance and efficiency of $Li-O_2$ batteries.

There have been many attempts to develop cathodes with high-performance for $Li-O_2$ batteries. Ottakam Thotiyl *et al.* have reported that a TiC cathode gives promising results in $Li-O_2$ batteries and reduces side reactions related to electrolyte degradation

* Address correspondence to yksun@hanyang.ac.kr, curtiss@anl.gov.

Received for review January 13, 2015 and accepted March 23, 2015.

10.1021/acsnano.5b00267

compared with carbon based cathode.[9] Lu *et al.* have reported on a cathode consisting of Pd nanoparticles on a carbon surface with an alumina coating on carbon defect sites. The low charge potential is achieved by a catalytic effect of the Pd nanoparticles and the Al_2O_3 coating preventing electrolyte decomposition on carbon defect sites.[5] To avoid parasitic reactions between carbon cathodes and Li_2O_2, Li *et al.* designed a Ru/ITO electrode. The advantage in using a noncarbon electrode is that it can avoid carbon electrode side reactions such as reactions with lithium peroxide to form lithium carbonate.[6] However, further research is needed to find more effective catalysts to reduce high overpotentials stemming from slow kinetics and energy loss in decomposition of Li_2O_2.

Herein, we introduce well dispersed molybdenum carbide nanoparticles onto carbon nanotubes as a cathode material for $Li-O_2$ batteries. Mo_2C is well-known as a competitive catalyst for the hydrogen evolution reaction (HER),[10] the water gas shift reaction (WGS),[11] and in fuel cells.[12] On the basis of this, we assumed that Mo_2C could also be a good catalyst for the oxygen evolution reaction (OER) in $Li-O_2$ batteries, and the carbon nanotubes could help the Mo_2C nanoparticles be an ORR catalyst due to its electrical conductivity. In this paper a Mo_2C/carbon nanotube composite as a cathode is demonstrated to reduce high over potentials during charge and improve the cycling performance of $Li-O_2$ batteries.

RESULTS AND DISCUSSION

The Mo_2C/carbon nanotube composite was synthesized by facile ball milling and calcinations. After calcination, the final product was investigated by X-ray diffraction (see Figure 1a) and compared with a pristine-carbon nanotube. Crystalline Mo_2C (JCPDS No. 65-8766) peaks appear in broad humps in the 18−28° range coming from the pristine-carbon nanotube. From this data, it is confirmed that Mo_2C was successfully synthesized on carbon nanotubes in the Mo_2C/carbon nanotube composite. The Raman spectra of the Mo_2C/carbon nanotube and pristine-carbon nanotube (see Figure 1b) both exhibit three peaks at ∼1345, ∼1570, and ∼2700 cm^{-1} corresponding to the D, G, and 2D carbon bands, respectively. The intensity ratio of D and G bands (D/G) is used to evaluate the disorder in the materials.[13] Compared to results in other papers,[13,14] our pristine-carbon nanotube (multiwall carbon nanotubes, Hanwha Nanotech) exhibits a higher ratio for the intensity of the D and G bands (D/G) much like the functionalized-carbon nanotube.[15] The D/G intensity ratio of the Mo_2C/carbon nanotube is 0.98 and the D/G ratio of the carbon nanotube is 1.19. Li *et al.* demonstrated that the appearance of the oxygen-containing functional groups promote the dispersion of Mo precursors.[16] Accordingly, our pristine-carbon nanotube should be suitable for synthesis of the Mo_2C/carbon nanotube. After synthesis of the Mo_2C/carbon nanotube, the D/G ratio decreased due to formation of Mo_2C on the surface of the carbon nanotubes.

On the basis of an N_2-sorption measurement (see Figure 1c), the specific surface area of the Mo_2C/carbon nanotube and pristine-carbon nanotube samples are 511.1 and 645.4 $m^2\,g^{-1}$, respectively. The lower surface area of the Mo_2C/carbon nanotube can be attributed to the presence of Mo_2C on the surface of the carbon nanotube. However, the specific surface area of the Mo_2C/carbon nanotube is still high compared to bulk Mo_2C powder (see Supporting Information, Figure S1a). This high surface area can provide sufficient space for Li_2O_2 formation and decomposition.[7,8,17]

According to SEM images of the Mo_2C/carbon nanotube (see Figure 2a), an entangled carbon nanotube structure can be seen similar to the pristine-carbon nanotube (see Figure 2b). These results are in agreement with the similar specific surface area of both samples in the BET data (see Figure 1c).

High resolution TEM was used to investigate the Mo_2C/carbon nanotube structure (see Figure 2c). The TEM images showed some nanoparticles attached to the carbon nanotubes. It was confirmed that these nanoparticles are Mo_2C by an additional EDX mapping analysis (the molybdenum is denoted by red dots) shown in Figure 2C. Compared to TEM and EDX data of purchased bulk Mo_2C powder (see Supporting Information, Figure S1b), the Mo_2C nanoparticles on the defect site of carbon nanotube are much smaller

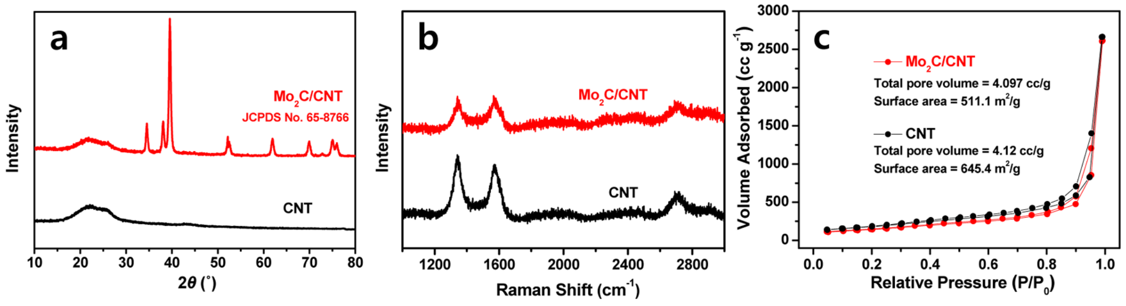

Figure 1. (a) XRD patterns, (b) Raman spectra, and (c) nitrogen adsorption−desorption isotherms of the Mo_2C/carbon nanotube and pristine-carbon nanotube.

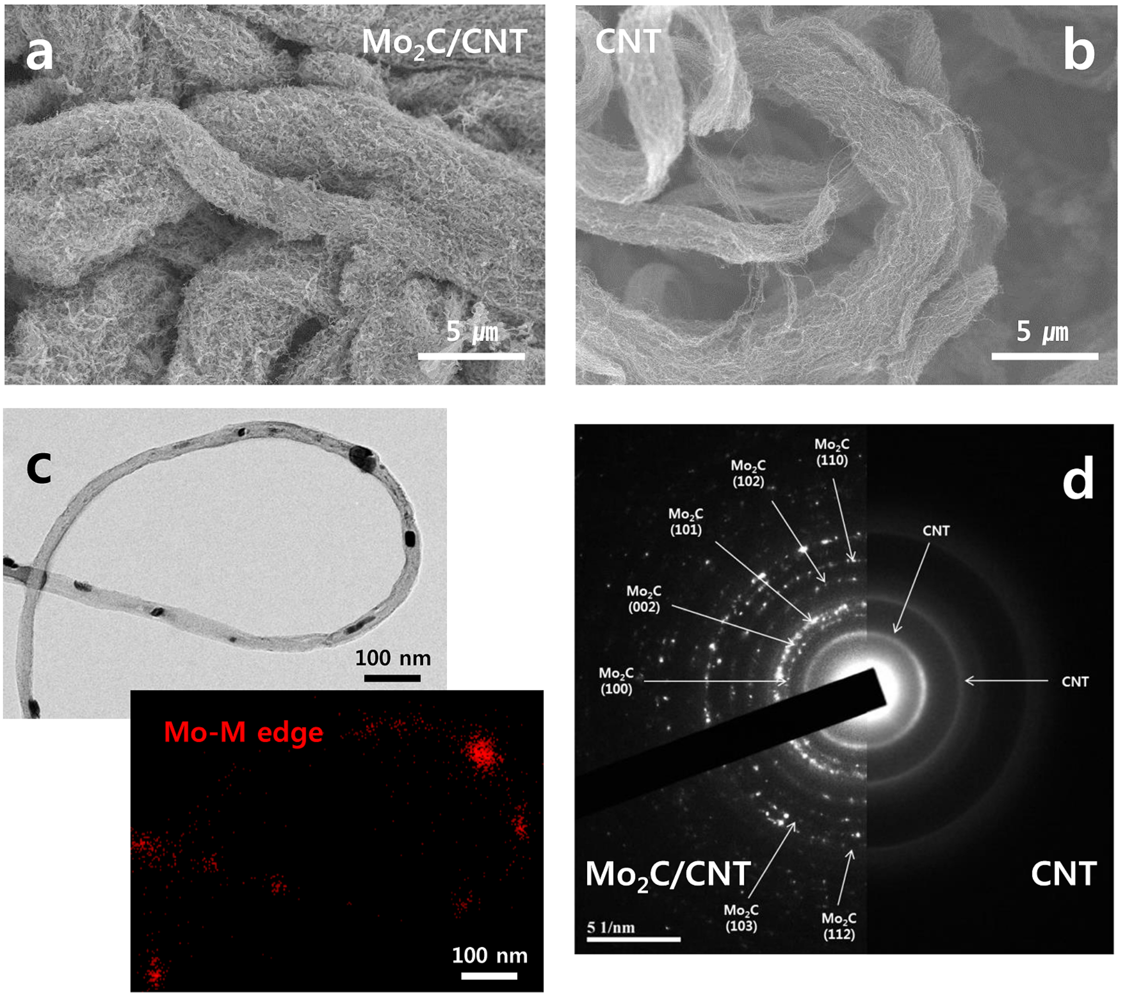

Figure 2. SEM images of (a) Mo_2C/carbon nanotube and (b) pristine-carbon nanotube; (c) TEM image and EDX maps (Mo elements) of the Mo_2C/carbon nanotube sample. (d) SAED patterns of the Mo_2C/carbon nanotube (left) and pristine-carbon nanotube (right).

and more well-dispersed. This point was further confirmed by the selected area electron diffraction (SAED) pattern shown on the left in Figure 2d. For comparison, the SAED pattern of a pristine-carbon nanotube is also shown on the right in Figure 2d. The SAED pattern of a Mo_2C/carbon nanotube showed the presence of a carbon nanotube and crystalline Mo_2C (JCPDS No. 65-8766), in accordance with the XRD data (see Figure 1a). With the above data, it was confirmed that a Mo_2C/carbon nanotube composite was successfully synthesized.

Pristine-carbon nanotube, bulk Mo_2C powder, and Mo_2C/carbon nanotube composite samples were tested as electrode materials in $Li-O_2$ batteries. While bulk Mo_2C powder and pristine-carbon nanotube electrodes exhibited relatively high overpotentials during discharge and charge (see Figure 3a), a remarkably lower overpotential and corresponding higher energy efficiency were observed for the Mo_2C/carbon nanotube composite electrode. The energy efficiency of the Mo_2C/carbon nanotube cathode was 88% compared to 53% for Mo_2C powder and 74% for pristine-carbon nanotube nanotubes. The polarization of the Mo_2C/carbon nanotube cathode was 0.47 V compared to 2.11 V for Mo_2C powder and 1.10 V for pristine-carbon nanotube nanotubes. As a consequence of the lowering of the overpotential, the cell cyclability was maintained up to the 150th cycle at a discharge capacity of 500 mA h g_{total}^{-1} (see Figure 3b).

In addition, the effects of current density change on the discharge/charge voltages of $Li-O_2$ batteries with the Mo_2C/carbon nanotube electrode were also investigated (see Figure 3c). With current densities at 100, 200, 500, and 1000 mA h g_{total}^{-1} 10 cycles were each run to a discharge depth of 500 mA h g_{total}^{-1}. The final discharge/charge voltages were 2.78/3.28 V, 2.76/3.41 V, 2.74/3.61 V, and 2.65/3.73 V at 100, 200, 500, and 1000 mA g_{total}^{-1}, respectively. We found the higher current density exhibited larger overpotentials compared to that of the cell operated at a current of 100 mA g_{total}^{-1}. However, even at 10 times higher current density (1000 mA g_{total}^{-1}), the polarization of the $Li-O_2$ battery with Mo_2C/carbon nanotube electrode was lower than that of a battery with only

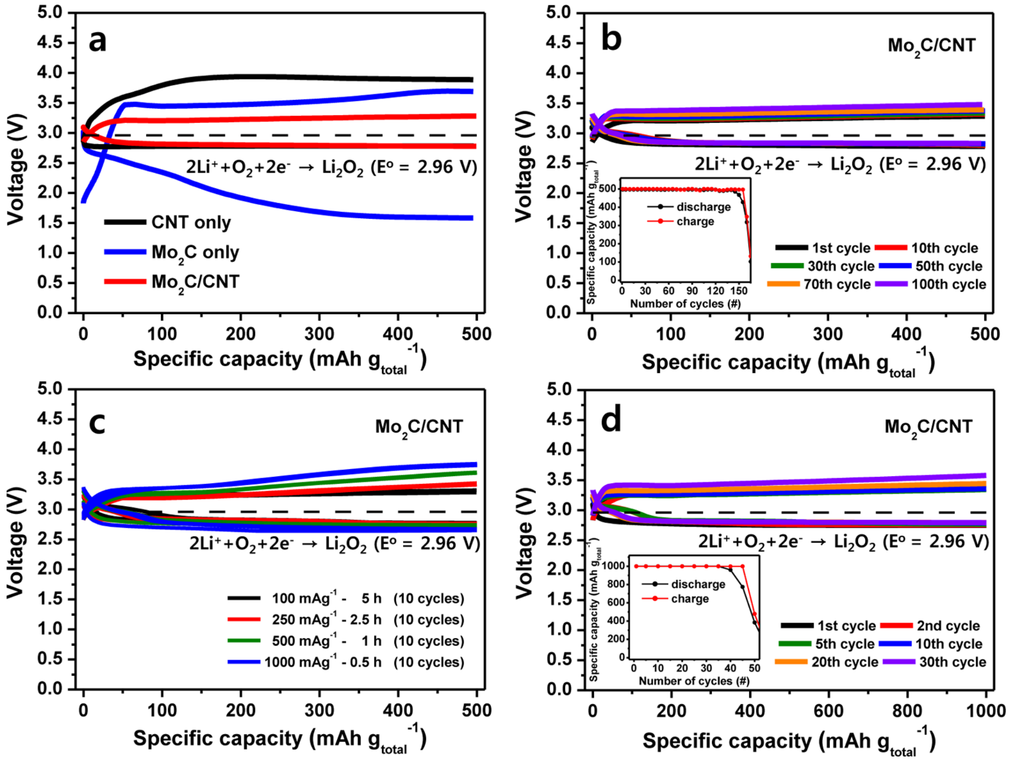

Figure 3. (a) The first discharge/charge profiles of the Li–O_2 batteries with pristine-carbon nanotube, Mo_2C, and Mo_2C/carbon nanotube electrodes at a discharge capacity of 500 mA h g_{total}^{-1} and a current density of 100 mA g_{total}^{-1}. (b) Cycling performance of the Li–O_2 battery with the Mo_2C/carbon nanotube electrode at a discharge capacity of 500 mA h g_{total}^{-1} and at a current density of 100 mA g_{total}^{-1}. (c) The first 10 cycles of Li–O_2 batteries with the Mo_2C/carbon nanotube electrode at current densities of 100, 200, 500, and 1000 mA g_{total}^{-1} with a discharge capacity of 500 mAh g_{total}^{-1}. (d) Cycling performance of the Li–O_2 battery with the Mo_2C/carbon nanotube electrode at a discharge capacity of 1000 mAh g_{total}^{-1} and at a current density of 200 mA g_{total}^{-1}.

the pristine-carbon nanotube electrode operated at a current of 100 mA g_{total}^{-1}. The improved performance of the Li–O_2 battery using a Mo_2C/carbon nanotube electrode was supported by cyclic voltammetry results (Supporting Information, Figure S2). Both the cathodic (oxygen reduction) and anodic reactions (oxygen evolution) of the Mo_2C/carbon nanotube electrode were more pronounced than for the pristine-carbon nanotube electrode.

Moreover, because the Mo_2C/carbon nanotube loading amount is larger than 1 mg cm^{-2}, the effective current flow in this battery system is greater than 1 mA, which is comparable to previously reported Li–O_2 battery systems.[9,18,19] The high sustained current in this cell configuration might be due to the unique *fruit*(Mo_2C)–*tree*(carbon nanotube) morphology, which combines the high electronic conductivity of the carbon nanotube and the superior catalytic activity of the Mo_2C nanosized particles. For these Mo_2C nanoparticles, we found that the thermodynamically dominant surfaces (i.e., (001) and (101)) of a Wulff shape of a Mo_2C particle[20] is metallic, similar to metallic Mo_2C bulk crystal according to DFT calculations (Supporting Information, Figure S5–S7). Thus, the good electronic conductivity needed for the oxygen reduction reaction (ORR) and oxygen evolution reaction (OER) can be facilitated by both the Mo_2C nanoparticles and carbon nanotubes. The Mo_2C nanoparticles on the surface of the carbon nanotubes may play an important role in the OER, whereas the carbon nanotubes might be a good ORR catalyst,[21] which leads to a low charge potential of the cell with cyclability up to ~30 cycles at a discharge depth of 1000 mA h g_{total}^{-1} (Figure 3d).

X-ray diffraction (XRD) and attenuated total reflection Fourier transform infrared (ATR-FTIR) measurements were conducted to identify the discharge products of Li–O_2 batteries with Mo_2C/carbon nanotubes. The XRD patterns of the Mo_2C/carbon nanotube electrodes for the first and 10th cycles at a current density of 100 mA g_{total}^{-1} are shown in Figure 4a. As compared with the XRD pattern of the fresh electrode, new diffraction peaks were observed in the discharged electrodes. Although these XRD peaks were very weak compared to the Mo_2C/carbon nanotube electrode, they can reasonably be assigned as the (100), (101), and (110) peaks of a Li_2O_2 crystal (as highlighted with black circles in Figure 4a).[9,18] The diffraction peaks of Li_2O_2 disappeared after the battery was recharged, which suggests that the discharge product Li_2O_2 is decomposed during the charging process. The ATR-FTIR spectra were obtained from the initial discharged and charged Mo_2C/carbon nanotube electrodes at a current density

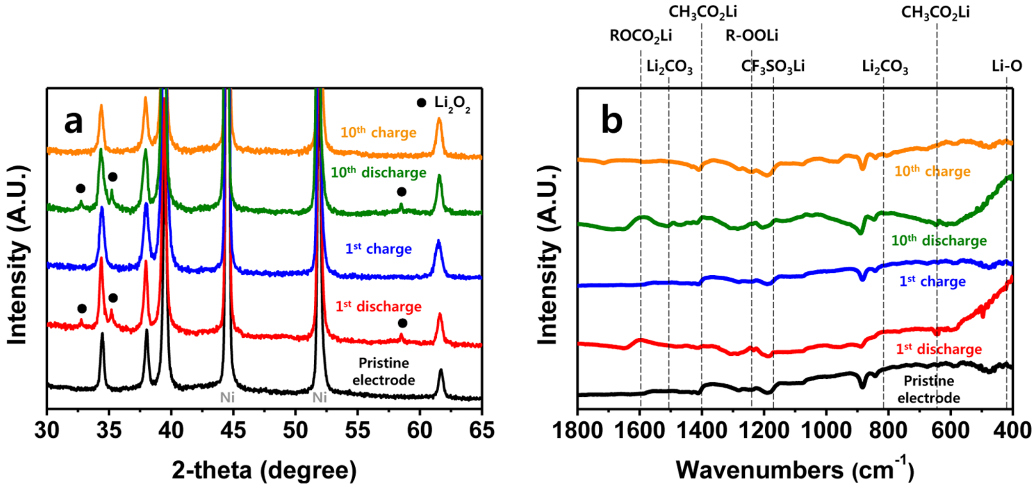

Figure 4. (a) XRD and (b) ATR-FTIR spectra of the fresh, discharged, and charged Mo_2C/carbon nanotube electrodes.

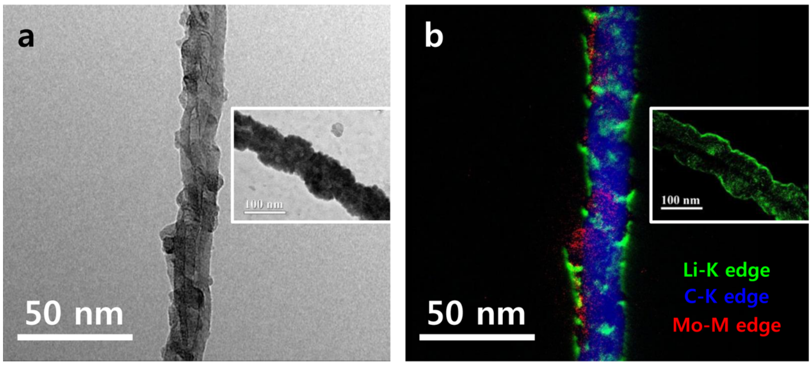

Figure 5. (a) HR-TEM image and (b) EF-TEM maps of the Mo_2C/carbon nanotube electrode after first discharge (discharge depth is 1000 mA h g_{total}^{-1}). A fully discharged Mo_2C/carbon nanotube electrode to 2.5 V is also presented in the inset data (length of scale bar in inset data is 100 nm).

of 100 mA g_{total}^{-1} (see Figure 4b). As shown, the ATR-FTIR absorption peaks at around 500 cm^{-1} in the discharged electrode can be assigned to Li_2O_2, that disappear in the charged electrode, which indicates the decomposition of Li_2O_2 during the charging process.[22,23]

The Li_2O_2 formed in the discharging process was directly observed by high resolution-TEM (HR-TEM) and energy filtered-TEM (EF-TEM). Figure 5a shows that some discharge products were deposited on the Mo_2C/carbon nanotube surface after the first cycle discharge. For identification, this spot was also analyzed by EF-TEM. As shown in Figure 5b, Li_2O_2, a carbon nanotube, and Mo_2C were visualized as green, blue, and red spots, respectively. (To make a distinction with the carbon nanotube, the Mo element of Mo_2C is denoted as red spots although it might also contain some carbon element in that area.) From this data, it is observed that the Li_2O_2 nanoparticles were deposited on the Mo_2C/carbon nanotube surface until reaching a capacity of 1000 mA h g_{total}^{-1}. This Li_2O_2 morphology was found to be similar to the reported result using a carbon nanotube electrode in the literature.[24,25] From some reported papers that used carbon nanotube electrodes, it was found that the Li_2O_2 is agglomerated and grown in a toroidal form with deeper discharge.[24,26] However, in our cell configuration after full discharge to 2.5 V (i.e., about 10000 mA h g_{total}^{-1}), the Li_2O_2 became thicker, but was still in a well dispersed layered form (not in a toroidal form) covering the Mo_2C/carbon nanotube as shown in the inset data of Figure 5a,b. This observation can be explained by the fact that Mo_2C nanoparticles on the carbon nanotube might mitigate the excessive accumulation of Li_2O_2 and result in efficient uniform dispersion of the Li_2O_2 layered product grown on the Mo_2C/carbon nanotube surface.[25]

The origin of the effectiveness of Mo_2C/carbon nanotube as a cathode in Li−O_2 batteries may relate to its surface chemistry and electronic properties based on DFT calculations and X-ray photoemission spectroscopy (XPS). From DFT calculations, we found that the O_2 molecules tend to be reduced on Mo_2C (001) and (101) surfaces that are dominant on the Wulff shape of Mo_2C nanoparticles.[20] For the two low energy Mo-terminated equivalent surfaces, that is, (001)-Mo and (101)-Mo surfaces (Supporting Information, Figures S6 and S7), the chemisorption of O_2 on the

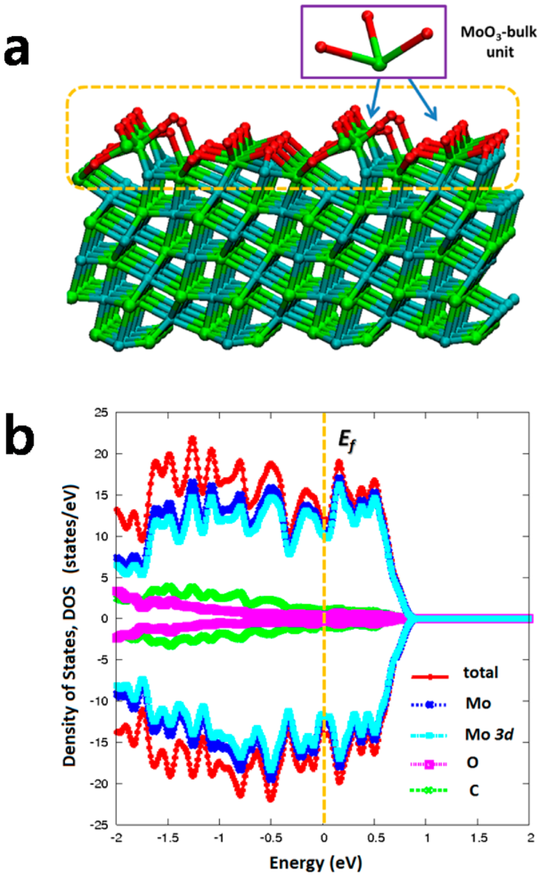

Figure 6. (a) The oxidized Mo_2C (101)-Mo surface with a MoO_3-like portion (the highlighted region shows a MoO_3-bulk unit-like configuration in the inset) on the top surface layer after the adsorbed O_2 molecules dissociate. (b) The electronic density of states (e-DOS) around the Fermi-level (E_f). The light-blue region is the Mo 3d projected e-DOS that dominate the e-DOS around the Fermi-level.

surfaces is exothermic (Figure S8 and S9). At both (001)-Mo and (101)-Mo surfaces, the decomposition of the O–O bond of chemisorbed O_2 molecules is exothermic and oxidizes the surface by forming new Mo–O bonds (Figures S8 and S9). For the thermodynamically most dominant surface, that is, the (101)-Mo surface, the dissociation of the adsorbed O_2 molecule on a clean (101)-Mo surface is thermodynamically very favorable with a formation energy, E_{form} of *ca.* −2.5 to −6.2 eV compared to E_{form} of *ca.* −1.3 eV for a (001)-Mo surface (Figures S8–S10). For a near fully oxidized Mo_2C (101)-Mo surface, the top surface is dominated by the Mo–O bonds analogous to the MoO_3 bulk-like layer shown in Figure 6. As shown in Figure 6, the surface chemistry and electronic properties of the oxidized Mo_2C are mainly dictated by the Mo 3d electronic states. The original metallic-like Mo_2C surface remains even after the surface is significantly oxidized.

For verification of the DFT predictions, XPS data were collected on a Mo_2C/carbon nanotube electrode as shown in Supporting Information, Figure S3. We found the surface of the as-received Mo_2C powder tends to be oxidized, and the MoO_3 and MoO_3/C-like states from XPS spectra are shown in Figure S3. Some MoO_2 is also present in the XPS data (Figure S3). The proportion of MoO_3/C increases on the 10th discharge and becomes the dominant species on the surface of the oxidized Mo_2C/carbon nanotube electrode. Thereafter, the XPS characters of the cathode surface are almost invariant during the cell cycling (*e.g.*, 50th cycle), with predominantly MoO_3/C-like character. To complement the surface-sensitive XPS data, the bulk-sensitive XRD data shows that the MoO_3-like feature in the cathode is not a layered orthorhombic crystalline MoO_3 bulk (*i.e.*, in *Pnma* space group),[27] but rather a noncrystalline amorphous phase that is formed on the surface of the Mo_2C nanoparticles as a thin layer. The evidence for this is that there are no peaks associated with crystalline MoO_3 as shown in Figure 4a. From DFT PBE calculations, the layered crystalline MoO_3 bulk is insulating (band gap, ~2 eV), whereas the noncrystalline amorphous phase of MoO_3 bulk is metallic (Supporting Information, Figure S11). Thus, we suspect that the formation of metallic noncrystalline MoO_3-like layers on the Mo_2C nanoparticles along with the carbon nanotubes are responsible for the low charge overpotentials and the high cyclability found in the Li–O_2 cells based on these new materials. The low overpotential Li_2O_2 formation/decomposition reaction found for these cathodes based on MoO_3/Mo_2C is similar to that reported for a TiO_2@TiC electrode in a Li–O_2 cell by Ottakam Thotiyl *et al.* recently.[9]

The Mo_2C/carbon nanotube electrode remains robust and stable even after 100 cycles at a capacity of 500 mA h g^{-1} with little electrolyte decomposition, as confirmed by H NMR analysis in Supporting Information, Figure S4. The structure of the TEGDME molecule is verified by the nearly identical integral area ratio (4:2:2:3) of the four H peaks coming from the cells before/after cycling (the pristine electrolyte was also checked individually)[9,28] and suggested that the TEGDME solvent is quite stable on the Mo_2C/carbon nanotube electrode interface during the discharge and charging processes. In addition, Bruce and coworkers in their recent report[22] have suggested that carbon materials are unstable on charging above 3.5 V, oxidatively decomposing to form Li_2CO_3. Carbon also promotes electrolyte decomposition to Li_2CO_3 and Li carboxylates during discharge and charge in a Li–O_2 battery at high voltages (above 3.5 V). To minimize these parasitic side reactions, the charge potential has to be less than 3.5 V, and we believe the Mo_2C/carbon nanotube composite electrode that operates at low charge potential (*i.e.*, less than 3.5 V) (Figure 3) in this study can help to minimize the serious electrolyte decomposition problem in a Li–O_2 cell. We did find some small peaks at 1.2 ppm and some small absorption peaks in the FTIR spectra (see Figure 4b) ascribed to lithium formate and acetate.[29] They may be attributed to some decomposition of the ether-based electrolyte during cycling. Although these negative results from NMR and IR data were quite negligible, we feel that finding more stable electrodes and electrolytes for lithium air battery systems is necessary and should be the subject of future research.

CONCLUSIONS

In summary, a Mo_2C/carbon nanotube composite cathode was found to have high electrical efficiency (88%) and reversibility (more than 100 cycles) for $Li-O_2$ batteries. The well dispersed Mo_2C nanoparticles on carbon nanotubes results in a nanolayered Li_2O_2 discharge product, which is easy to decompose with a low charge potential. Most importantly, the $Li-O_2$ battery using an as-prepared Mo_2C/carbon nanotube electrode could be cycled repeatedly with dramatically low charge potential (3.25−3.4 V). We suspect that the formation of metallic noncrystalline MoO_3-like layers on the Mo_2C nanoparticles along with the carbon nanotubes are responsible for the low charge overpotentials and high cyclability. Although no electrolyte and electrode can be 100% stable yet, we expect that this effective composite cathode can be a good reference to help improve the electrical efficiency and cyclability in the $Li-O_2$ battery system.

METHODS

Synthesis of Mo_2C/Carbon Nanotube. Carbon nanotube-supported molybdenum carbides (Mo_2C/carbon nanotube) were prepared by carbothermal reduction of carbon-supported molybdenum trioxde (MoO_3, ≥ 99.5%, Aldrich).[30] The typical procedure for preparing the carbides is as follows: The starting materials (MoO_3 and carbon nanotube) were accurately weighed according to the stoichiometric amounts in for the equation ($2MoO_3 + 7C \rightarrow Mo_2C + 6CO$) and mixed by ball milling for 24 h. The rotation speed and ball-to-powder weight ratio were 300 rpm and 20:1. To protect the materials from oxidation, the milling operation was carried out under high purity of argon atmosphere. Then, for carbothermal reduction, the milled sample was annealed in a furnace with a 100 mL min^{-1} Ar flow from room temperature to 950 °C at a rate of 10 °C min^{-1} and then held at 950 °C for 1 h. Ar was kept flowing through the reactor when the furnace was cooled to ambient temperature. The weight ratio of Mo_2C and carbon nanotube in the composite is Mo_2C/carbon nanotube = 8:2 (checked by thermogravametric analysis with nitrogen) Carbon nanotubes (multiwall carbon nanotubes, Hanwha Nanotech)-supported molybdenum carbide and graphite (99.9995%, Alfa Aesar)-supported molybdenum carbide were prepared by the same procedure as above. Meanwhile, bulk Mo_2C (≥99.5%, Alfa Aesar) was purchased.

Preparation of $Li-O_2$ cells. A mixture containing 80 wt % of carbide material (Mo_2C/carbon nanotube or bulk Mo_2C) and 20 wt % of polytetrafluoroethylene (PTFE) binder was well mixed in a *N*-methyl-2-pyrrolidone (NMP) solvent and then coated onto Ni foam (thickness, 200 μm) in a dry room. The coated electrodes were dried at 100 °C under vacuum for 12 h to remove the residual solvent and were cut to 1.4 cm in diameter. These air electrodes (loading of cathode materials on the Ni foam was about 1.7 mg), a glass fiber separator (GF/C, Whatman), and lithium metal foil (thickness, 400 μm) were assembled in a R2032 coin-type cell. A solution of 1 M lithium triflate ($LiCF_SO_3$) in tetraethylene glycol dimethyl ether (TEGDME) was used as the electrolyte. Solvents were stored over 4 Å molecular sieves in an Ar-filled glovebox (final water content of <10 ppm, determined using a Mettler-Toledo Karl Fischer titration). All cell assembly procedures were done in an argon-filled glovebox (water and oxygen contents are less than 0.1 ppm). Before the test, cells were placed in an oxygen-filled chamber with a pressure slightly higher than 1 atm at room temperature and stabilized for 1 h.

Characterizations. The electrochemical properties were measured by a VMP3 Biologic Instruments meter using a galvanostatic cycling test with a time-controlled mode at a current density of 100 mA g^{-1} for 5 h (and also 200 mA g^{-1} for 5 h). All discharge/charge capacities were calculated based on per-gram units of the carbide and composite materials (only Mo_2C, only carbon nanotube, and Mo_2C/carbon nanotube composite, respectively). Raman spectra were obtained on a Micro-Raman spectrophotometer (MonoRa750i, Optron). The surface area and porosity of carbide materials were measured with automated gas sorption analyzer (autosorb iQ, Quantachrome) using nitrogen gas as the adsorbate at a temperature of 77 K. The specific surface area was calculated using the Brunauer−Emmett−Teller (BET) method. A field emission scanning electron microscope (FE-SEM, S-4800, Hitachi) and a high-resolution transmission electron microscopy (HR-TEM, JEM-2010, JEOL) were employed to observe the morphology of the air electrode materials and discharge products. EDX (energy dispersive X-ray spectroscopy) and EF(energy filtered)-TEM mapping were analyzed with same TEM instrument. The discharged and charged electrodes were protected from exposure to air during the transfer to the SEM and TEM chamber with a portable vacuum oven applied in the glovebox. The carbide materials and air electrodes after the cycle test were measured by using the X-ray diffraction instrument (XRD, D/MAX 2500, Rigaku) with a Cu Kα radiation source within 2θ of 10.0° to 80.0° at a scan rate of 1°/min. Fourier transform infrared instrument (FTIR, Nicolet iS50, Thermo) was employed, and analysis was fulfilled in the N_2 filled glovebox. However, it is hard to confirm the discharge product within transmission mode because carbon materials easily absorb the infrared. Making pellets can also damage the discharge product in the electrode. An attenuated total reflectance (ATR) equipment for the FTIR instrument was set up and used to check the discharge product. Before the analysis of the electrode after discharge and charge, the electrodes were washed by TEGDME solvent and dried under vacuum at least for 2 days.

DFT Calculation. To model the catalytic role played by the Mo_2C nanoparticles in the experiments, the thermodynamically abundant surfaces of Mo_2C Wulff crystal predicted in a recent study are considered.[20] To model the two dominant surfaces (*i.e.*, (001) and (101)), Mo_2C and MoO_3 bulk crystals, the simulation is carried out based on Density Functional Theory (DFT) calculations with plane wave basis sets as implemented in the VASP code.[31] All the calculations were spin-polarized and carried out using the gradient corrected exchange-correlation functional of Perdew, Burke, and Ernzerhof (PBE)[32] under the projector augmented wave (PAW) method, with plane wave basis sets up to a kinetic energy cutoff of 400 eV. The PAW method[33] was used to represent the interaction between the core and valence electrons, and the Kohn−Sham valence states (*i.e.*, 2s for Li, 2s 2p for C and O, and 4p 5s 4d for Mo) are expanded in plane wave basis sets. The convergence criterion of the total energy was set to be within 1×10^{-5} eV for the K-point integration, and all the atoms and geometries were optimized until the residual forces became less than 1×10^{-2} eV/Å. For the hexagonal Mo_2C and orthorhombic MoO_3 crystalline solid, the optimized structure obtained after the full geometry relaxation was carried out within a K-point 5 × 5 × 5 grid. For all the relevant surfaces calculations, all the simulations (*i.e.*, including O_2 adsorption on surfaces) were carried out within a K-point 5 × 5 × 1 grid. For each of the modeled surfaces (*i.e.*, (001) and (101) surface), two different surface terminations (*i.e.*, Mo-term and C-term) have been studied and all the surface thicknesses are about 12−15 Å throughout the simulation to ensure the required energy convergence.

To model a noncrystalline amorphous structure of MoO_3 bulk, two different approaches were used. The approaches were based on *ab Initio* Molecular Dynamics (AIMD) simulations using an NVT-ensemble with a time step of 1 fs. For one model, the amorphous MoO_3 structure is obtained using "heat-and-quench" of a MoO_3 crystal to $T \approx 4000$ K with rapid cooling to 300 K at a rate of $\sim 5.8 \times 10^{15}$ K/s. The final optimized geometry is obtained by taking the final thermal equilibrated configuration ($\sim$1.0 ps at $T \approx 300$ K) after full geometry relaxation. For the other model amorphous MoO_3 structure, the initial structure was generated by randomly placing 32 basic MoO_3 units into an orthorhombic cell. After the initial full cell relaxation, the system is then thermally equilibrated at $T = 300$ K, and the final optimized geometry is obtained by taking the final thermal equilibrated configuration (after $\approx$ 1.5 ps) after full geometry relaxation. As shown in Supporting Information, Figure S11, both amorphous MoO_3 structures are found to be similar (*i.e.*, similar in Mo−O and Mo−Mo distributions). In addition they are both metallic and only $\sim$0.20−0.30 eV/(MoO_3-unit) less stable than the MoO_3 crystal.

Conflict of Interest: The authors declare no competing financial interest.

Supporting Information Available: SEM, TEM, BET data of Mo_2C bulk powder, XPS spectra of Mo_2C/carbon nanotube cathode, H NMR data of electrolyte before and after cycling test, and supplementary DFT calculation. This material is available free of charge *via* the Internet at http://pubs.acs.org.

Acknowledgment. This work at Hanyang University was supported by the Human Resources Development program (No. 20124010203310) of the Korea Institute of Energy Technology Evaluation and Planning (KETEP) grant funded by the Korea government Ministry of Trade, Industry and Energy and also supported by the Global Frontier R&D Program (2013M3A6B1078875) of the Center for Hybrid Interface Materials (HIM) funded by the Ministry of Science, ICT & Future Planning. The work at Argonne National Laboratory was supported by the U.S. Department of Energy under Contract DE-AC0206CH11357 from the Vehicle Technologies Office, Department of Energy, Office of Energy Efficiency and Renewable Energy (K.A.) and Division of Materials Science and Engineering, Basic Energy Science (K.C.L. and L.A.C.). We also acknowledge grants of computer time through the ALCF Fusion and Blues Clusters at Argonne National Laboratory.

REFERENCES AND NOTES

1. Bruce, P. G.; Freunberger, S. A.; Hardwick, L. J.; Tarascon, J. M. Li−O_2 and Li−S Batteries with High Energy Storage. *Nat. Mater.* **2012**, *11*, 19–29.
2. Jung, H. G.; Hassoun, J.; Park, J. B.; Sun, Y. K.; Scrosati, B. An Improved High-Performance Lithium−Air Battery. *Nat. Chem.* **2012**, *4*, 579–585.
3. Lu, Y. C.; Shao-Horn, Y. Probing the Reaction Kinetics of the Charge Reactions of Nonaqueous Li−O_2 Batteries. *J. Phys. Chem. Lett.* **2013**, *4*, 93–99.
4. Xu, J. J.; Wang, Z. L.; Xu, D.; Zhang, L. L.; Zhang, X. B. Tailoring Deposition and Morphology of Discharge Products towards High-Rate and Long-Life Lithium-Oxygen Batteries. *Nat. Commun.* **2013**, *4*, 2438–2449.
5. Lu, J.; Lei, Y.; Lau, K. C.; Luo, X.; Du, P.; Wen, J.; Assary, R. S.; Das, U.; Miller, D. J.; Elam, J. W.; *et al.* A Nanostructured Cathode Architecture for Low Charge Overpotential in Lithium−Oxygen Batteries. *Nat. Commun.* **2014**, *5*, 2383–2391.
6. Li, F.; Tang, D. M.; Chen, Y.; Golderg, D.; Kitaura, H.; Zhang, T.; Yamada, A.; Zhou, H. Ru/ITO: A Carbon-Free Cathode for Nonaqueous Li−O_2 Battery. *Nano Lett.* **2013**, *13*, 4702–4707.
7. Guo, Z.; Zhou, D.; Dong, X.; Qiu, Z.; Wang, Y.; Xia, Y. Ordered Hierarchical Mesoporous/Macroporous Carbon: A High-Performance Catalyst for Rechargeable Li−O_2 Batteries. *Adv. Mater.* **2013**, *25*, 5668–5672.
8. Wu, D.; Guo, Z.; Yin, X.; Pang, Q.; Tu, B.; Zhang, L.; Wang, Y. G.; Li, Q. Metal−Organic Frameworks as Cathode Materials for Li−O_2 Batteries. *Adv. Mater.* **2014**, *26*, 3258–3262.
9. Thotiyl, M. M. O.; Freunberger, S. A.; Peng, Z.; Chen, Y.; Liu, Z.; Bruce, P. G. A Stable Cathode for the Aprotic Li−O_2 Battery. *Nat. Mater.* **2013**, *12*, 1050–1056.
10. Chen, W. F.; Wang, C. H.; Sasaki, K.; Marinkovic, N.; Xu, W.; Muckerman, J. T.; Zhu, Y.; Adzic, R. R. Highly Active and Durable Nanostructured Molybdenum Carbide Electrocatalysts for Hydrogen Production. *Energy Environ. Sci.* **2013**, *6*, 943–951.
11. Schweitzer, N. M.; Schaidle, J. A.; Ezekoye, O. K.; Pan, X.; Linic, S.; Thompson, L. T. High Activity Carbide Supported Catalysts for Water Gas Shift. *J. Am. Chem. Soc.* **2011**, *133*, 2378–2381.
12. Matsumoto, T.; Nagashima, Y.; Yamazaki, T.; Nakamura, J. Fuel Cell Anode Composed of Mo_2C Catalyst and Carbon Nanotube Electrodes. *Electrochem. Solid-State Lett.* **2006**, *9*, A160–A162.
13. Chuang, C. C.; Huang, J. H.; Chen, W. J.; lee, C. C.; Chang, Y. Y. Role of Amorphous Carbon Nanowires in Reducing the Turn-On Field of Carbon Films Prepared by Microwave-Heated CVD. *Diamond Relat. Mater.* **2004**, *13*, 1012–1016.
14. Han, J.; Duan, J.; Chen, P.; Lou, H.; Zheng, X.; Hong, H. Nanostructured Molybdenum Carbides Supported on Carbon Nanotubes as Efficient Catalysts for One-Step Hydrodeoxygenation and Isomerization of Vegetable Oils. *Green Chem.* **2011**, *13*, 2561–2568.
15. Steven, E.; Saleh, W. R.; Lebedev, V.; Acquah, S. F. A.; Laukhin, V.; Alamo, R. G.; Brooks, J. S. Carbon Nanotubes on a Spider Silk Scaffold. *Nat. Commun.* **2013**, *4*, 2435–2442.
16. Li, X.; Ma, D.; Chen, L.; Bao, X. Fabrication of Molybdenum Carbide Catalysts Over Multiwalled Carbon Nanotubes by Carbothermal Hydrogen Reduction. *Catal. Lett.* **2007**, *116*, 63–69.
17. Meini, S.; Piana, M.; Beyer, H.; Schwammlein, J.; Gasteiger, H. A. Effect of Carbon Surface Area on First Discharge Capacity of Li-O_2 Cathodes and Cycle-Life Behavior in Ether-Based Electrolytes. *J. Electrochem. Soc.* **2012**, *159*, A2135–A2142.
18. Jian, Z.; Liu, P.; Li, F.; He, P.; Guo, X.; Chen, M.; Zhou, H. Core−Shell-Structured CNT@RuO_2 Composite as a High-Performance Cathode Catalyst for Rechargeable Li−O_2 Batteries. *Angew. Chem., Int. Ed.* **2014**, *53*, 442–446.
19. Lim, H. D.; Song, H.; Kim, J.; Gwon, H.; Bae, Y.; Park, K. Y.; Hong, J.; Kim, H.; Kim, T.; Kim, Y. H.; *et al.* Superior Rechargeability and Efficiency of Lithium−Oxygen Batteries: Hierarchical Air Electrode Architecture Combined with a Soluble Catalyst. *Angew. Chem., Int. Ed.* **2014**, *53*, 3926–3931.
20. Wang, T.; Liu, X.; Wang, S.; Huo, C.; Li, Y. W.; Wang, J.; Jiao, H. Stability of β-Mo_2C Facets from ab Initio Atomistic Thermodynamics. *J. Phys. Chem. C* **2011**, *115*, 22360–22368.
21. Kannan, R.; Bipinlal, U.; Kurungot, S.; Pillai, V. K. Enhanced Electrocatalytic Performance of Functionalized Carbon Nanotube Electrodes for Oxygen Reduction in Proton Exchange Membrane Fuel Cells. *Phys. Chem. Chem. Phys.* **2011**, *13*, 10312–10317.
22. Thotiyl, M. M. O.; Freunberger, S. A.; Peng, Z.; Bruce, P. G. The Carbon Electrode in Nonaqueous Li-O_2 Cells. *J. Am. Chem. Soc.* **2013**, *135*, 494–500.
23. Mizuno, F.; Takechi, K.; Higashi, S.; Shiga, T.; Shiotsuki, T.; Takazawa, N.; Sakurabayashi, Y.; Okazaki, S.; Nitta, I.; Kodama, T.; *et al.* Cathode Reaction Mechanism of Nonaqueous Li−O_2 Batteries with Highly Oxygen Radical Stable Electrolyte Solvent. *J. Power Sources* **2013**, *228*, 47–56.
24. Lim, H. D.; Park, K. Y.; Song, H.; Jang, E. Y.; Gwon, H.; Kim, J.; Kim, Y. H.; Lima, M. D.; Robles, R. O.; Leprõ, X.; *et al.* Enhanced Power and Rechargeability of a Li−O_2 Battery Based on a Hierarchical-Fibril CNT Electrode. *Adv. Mater.* **2013**, *25*, 1348–1352.
25. Yilmaz, E.; Yogi, C.; Yamanaka, K.; Ohta, T.; Byon, H. R. Promoting Formation of Noncrystalline Li_2O_2 in the Li−O_2

Battery with RuO_2 Nanoparticles. *Nano Lett.* **2013**, *13*, 4679–4684.

26. Mitchell, R. R.; Gallant, B. M.; Shao-Horn, Y.; Thompson, C. V. Mechanisms of Morphological Evolution of Li_2O_2 Particles during Electrochemical Growth. *J. Phys. Chem. Lett.* **2013**, *4*, 1060–1064.
27. Stoyanova, A.; Iordanova, R.; Mancheva, M.; Dimitriev, Y. Synthesis and Structural Characterization of MoO_3 Phases Obtained from Molybdic Acid by Addition of HNO_3 and H_2O_2. *J. Optoelectron. Adv. Mater.* **2009**, *11*, 1127–1131.
28. Zhao, G.; Mo, R.; Wang, B.; Zhang, L.; Sun, K. Enhanced Cyclability of Li−O_2 Batteries Based on TiO_2 Supported Cathodes with No Carbon or Binder. *Chem. Mater.* **2014**, *26*, 2551–2556.
29. Choi, N. S.; Jeong, G.; Koo, B.; Lee, Y. W.; Lee, K. T. Tris(pentafluorophenyl) Borane-Containing Electrolytes for Electrochemical Reversibility of Lithium Peroxide-Based Electrodes in Lithium−Oxygen Batteries. *J. Power Sources* **2013**, *225*, 95–100.
30. Khabbaz, S.; Raouf, A. H.; Ataie, A.; Saghafi, M. Effect of Processing Parameters on the Mechanochemical Synthesis of Nanocrystalline Molybdenum Carbide. *Int. J. Refract. Met. Hard Mater.* **2013**, *41*, 402–407.
31. Kresse, G.; Furthmuller, J. Efficiency of *ab-Initio* Total Energy Calculations for Metals and Semiconductors Using a Plane-Wave Basis Set. *Comput. Mater. Sci.* **1996**, *6*, 15–50.
32. Perdew, J. P.; Burke, K.; Ernzerhof, M. Generalized Gradient Approximation Made Simple. *Phys. Rev. Lett.* **1996**, *77*, 3865–3868.
33. Blöchl, P. E. Projector Augmented-Wave Method. *Phys. Rev. B* **1994**, *50*, 17953–17979.